The Astrophysical Journal Letters, 896:L37 (7pp), 2020 June 20 https://doi.org/10.3847/2041-8213/ab9898

Spectropolarimetric Properties of Swift J1818.0–1607: A 1.4 s Radio Magnetar

Marcus E. Lower[1,2], Ryan M. Shannon[1,3], Simon Johnston[2], and Matthew Bailes[1,3]
[1] Centre for Astrophysics and Supercomputing, Swinburne University of Technology, PO Box 218, Hawthorn, VIC 3122, Australia; mlower@swin.edu.au
[2] CSIRO Astronomy and Space Science, Australia Telescope National Facility, Epping, NSW 1710, Australia
[3] OzGrav: The ARC Centre of Excellence for Gravitational-wave Discovery, Hawthorn, VIC 3122, Australia
Received 2020 April 23; revised 2020 May 22; accepted 2020 June 1; published 2020 June 18

Abstract

The soft-gamma repeater Swift J1818.0−1607 is only the fifth magnetar found to exhibit pulsed radio emission. Using the Ultra-Wideband Low receiver system of the Parkes radio telescope, we conducted a 3 hr observation of Swift J1818.0−1607. Folding the data at a rotation period of $P = 1.363$ s, we obtained wideband polarization profiles and flux density measurements covering radio frequencies between 704 and 4032 MHz. After measuring, and then correcting for the pulsar's rotation measure of 1442.0 ± 0.2 rad m^{-2}, we find the radio profile is between 80% and 100% linearly polarized across the wide observing band, with a small amount of depolarization at low frequencies that we ascribe to scatter broadening. We also measure a steep spectral index of $\alpha = -2.26^{+0.02}_{-0.03}$ across our large frequency range, a significant deviation from the flat or inverted spectra often associated with radio-loud magnetars. The steep spectrum and temporal rise in flux density bears some resemblance to the behavior of the magnetar-like, rotation-powered pulsar PSR J1119−6127. This leads us to speculate that Swift J1818.0−1607 may represent an additional link between rotation-powered pulsars and magnetars.

Unified Astronomy Thesaurus concepts: Magnetars (992); Neutron stars (1108); Pulsars (1306); Radio pulsars (1353)

1. Introduction

Magnetars are a rare class of relatively slow rotating neutron star that are inferred to possess some of the strongest magnetic fields in the universe. Until recently, only 4 of the 23 confirmed magnetars[4] (Olausen & Kaspi 2014) were seen to exhibit pulsed radio emission (Camilo et al. 2006, 2007a; Levin et al. 2010; Eatough et al. 2013; Shannon & Johnston 2013). Unlike standard rotation-powered pulsars, the radio pulses seen from these magnetars have generally flat spectra and display highly variable flux densities over timescales ranging between seconds to months (Camilo et al. 2007b; Lazaridis et al. 2008). Their single pulses are often comprised of many burst-like subpulses that display a remarkable range of temporal phenomenology. These subpulses have drawn comparisons to similar "spiky" emission seen in high magnetic field strength pulsars (Weltevrede et al. 2011), rotating radio transients (McLaughlin et al. 2006), and fast radio bursts (FRBs; Pearlman et al. 2018). Observations covering wide radio frequency bands may shed light on their magnetospheric conditions following outbursts, in particular whether the same processes that produce coherent, highly polarized emission in rotation-powered pulsars are also responsible for pulsed radio emission from magnetars.

Recently a fifth radio-bright magnetar was identified. Swift J1818.0−1607 was discovered by the Swift space observatory following the detection of a gamma-ray outburst by the Burst Alert Telescope on MJD 58920 (2020-03-12-21:16:47 UT). The burst was quickly localized to an X-ray point source by the onboard X-ray telescope (Evans et al. 2020). Observations by the Neutron star Interior Composition ExploreR found the source exhibited pulsed X-ray emission with a periodicity of 1.36 s (Enoto et al. 2020). Two days after the initial outburst, highly linearly polarized radio pulsations were detected with a dispersion measure (DM) of 706 ± 4 pc cm^{-3} during follow-up observations by the 100 m Effelsberg radio telescope observing in a band centered on 1.37 GHz (Karuppusamy et al. 2020). Continued timing provided an initial measurement of the spin-period derivative, $\dot{P} = 9 \pm 1 \times 10^{-11}$ (Esposito et al. 2020), firmly cementing its status as the fastest rotating, and possibly the youngest magnetar found to date. Observations performed at multiple radio wavelengths indicated the magnetar's radio emission has a steep spectral index (Gajjar et al. 2020; Lower & Shannon 2020). This is similar to the observed radio spectra of many ordinary, rotation-powered radio pulsars, but significantly differs from the flat or inverted spectra of the four other radio-loud magnetars. The apparently low surface temperature (Esposito et al. 2020) and lack of coincident supernova remnant, indicate Swift J1818.0−1607 may be significantly older than implied by its characteristic age of 240–310 yr, and may represent a transitional link between magnetars and the population of high B-field, rotation-powered pulsars. In particular, the reported spectral flattening by Majid et al. (2020) may indicate a possible link to the 2016 magnetar-like outburst of PSR J1119−6127 (Majid et al. 2017).

In this Letter we report on observations of Swift J1818.0−1607 using the ultra-wideband low (UWL) receiver system (-Hobbs et al. 2020) of the CSIRO 64 m Parkes radio telescope. Using Bayesian inference techniques, we measured the broadband properties of the time-averaged polarization spectrum and analyzed the sample of bright single pulses observed throughout the approximately 3 hr long observation. We then compare these results to previous observations of the four other radio-loud magnetars and the general pulsar population. Finally, we discuss the potential evolutionary pathways of Swift J1818.0−1607.

2. Observation and Analysis

We conducted a 10,473 s observation of Swift J1818.0−1607 on MJD 58939 using the Parkes UWL receiver (Hobbs et al. 2020) under the target of opportunity request PX057 (PI: Lower). Pulsar search-mode data with 128 μs sampling

[4] http://www.physics.mcgill.ca/~pulsar/magnetar/main.html

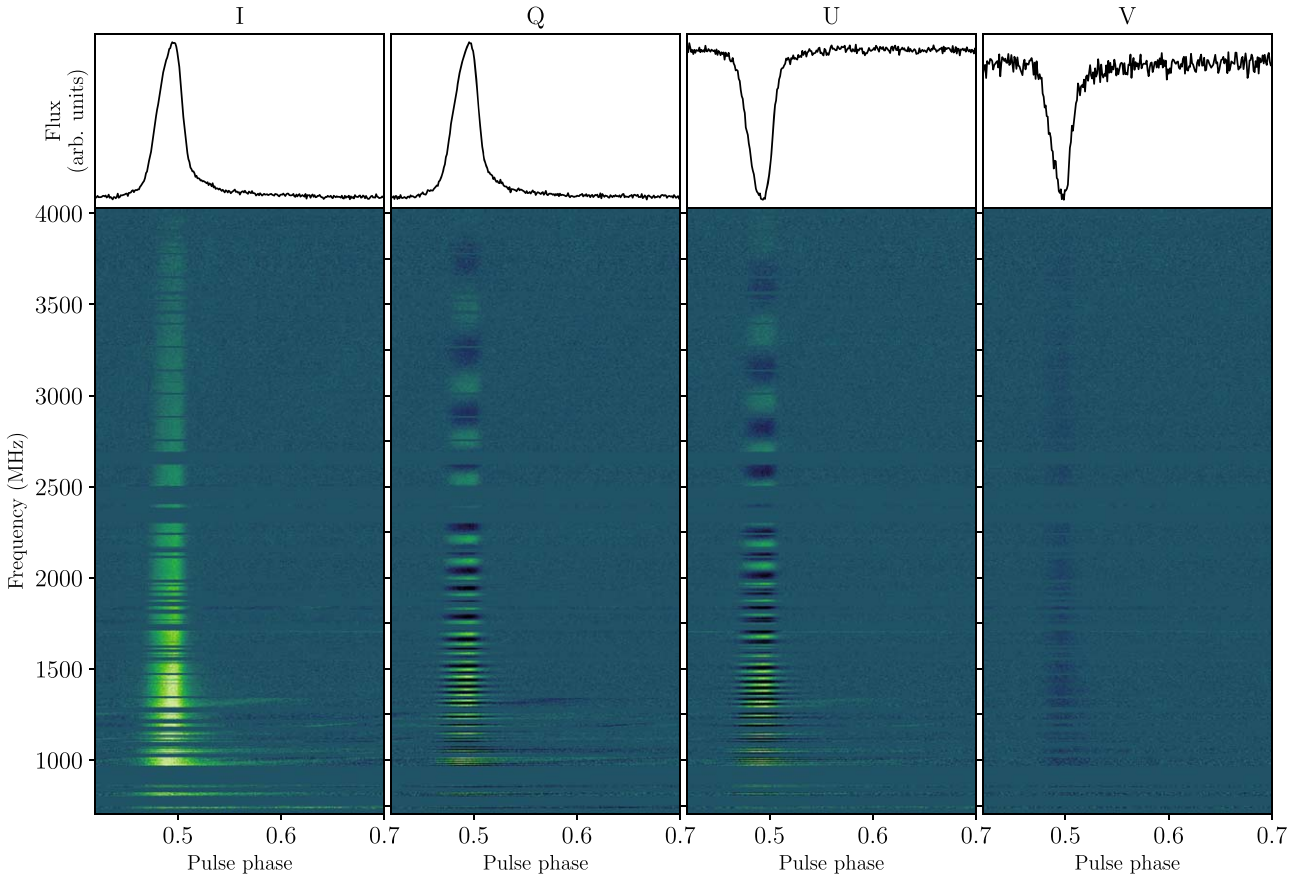

Figure 1. Faraday-corrected average polarization profiles (top) and uncorrected, time-averaged polarization spectra (bottom) of Swift J1818.0−1607. All four Stokes parameters are plotted with 2 MHz spectral resolution and 0.67 ms temporal resolution. The large rotation measure of 1442.0 ± 0.2 rad m^{-2} is clearly visible in Stokes Q and U. Horizontal gaps in each panel represent frequency channels that were excised due to RFI contamination. Some broadband sweeps of RFI remain visible below 1300 MHz.

covering the full UWL band from 704 to 4032 MHz with full Stokes information were recorded using the MEDUSA backend and coherently dedispersed on a channel-by-channel basis at a DM of 700 pc cm^{-3} to minimize dispersive smearing of the pulse profile. Note the profiles shown in Figure 1 have been dedispersed using the inferred DM of 706.0 pc cm^{-3} from Section 2.3. The data were then folded at the pulse period of the magnetar using `DSPSR` (van Straten & Bailes 2011) and saved to a `psrfits` (Hotan et al. 2004) format archive with 1024 phase bins, and 3328 frequency channels with 1 MHz frequency resolution. Approximately 35% of the 3328 frequency channels were heavily contaminated by radio frequency interference (RFI), and were subsequently excised using the standard `paz` and `pazi` tools in `PSRCHIVE` (Hotan et al. 2004; van Straten et al. 2012). The data were flux and polarization calibrated in the same manner as Dai et al. (2019), with the exception that we used the radio galaxy PKS B0407−658 as a flux density reference instead of 3C 218. Unlike 3C 218, PKS B0407−658 is not resolved by Parkes above ∼3 GHz, making it a more reliable calibrator for the UWL. We used an observation of a linearly polarized noise diode prior to observing the magnetar, in addition to on- and off-source observations of PKS B0407−658 taken on MJD 58638 to measure the noise diode brightness and to correct the phase and absolute gain of the system. We note that any leakage terms were not corrected for, which may be of order 5% toward the top of the band.

2.1. Profile Phenomenology and Flux Density

Dynamic spectra showing the four Stokes parameters across the continuous 704–4032 MHz UWL band are displayed in Figure 1. The pulse profile shows clear evidence of a steep negative gradient in flux density, and can be described as the superposition of two Gaussian components (G_1 and G_2 hereafter). The narrower G_2 component appears brighter toward the lower end of the UWL band, indicating it has a steeper spectral index than G_1.

We further analyzed the profile by dividing the data into 13 subbands, each having 256 MHz of bandwidth. These subbands were then averaged in frequency and polarization before being fit with a two-component Gaussian profile convolved with a one-sided exponential pulse broadening function

$$f(t) = \sum_{i=1}^{2} \frac{1}{\sqrt{2\pi\sigma_i^2}} e^{-(t-\mu_i)^2/2\sigma_i^2} \circledast e^{-t/\tau_{\rm sc}}, \quad (1)$$

where μ_i and σ_i are the centroids and widths of the $i^{\rm th}$ Gaussian component, $\circledast$ indicates a convolution, and $\tau_{\rm sc}$ is the scattering timescale. The resulting posterior probability distributions were sampled using the `bilby` software package (Ashton et al. 2019) as a front end to the `dynesty` nested sampling algorithm (Speagle 2020). Initially we fit the subbands assuming uniform priors on the widths of the profile components G_1 and G_2. However, we found the component widths were highly covariant with the scattering timescale, to

Table 1
Scatter Broadening (τ_{sc}), Period-averaged Flux Density (S_ν) Measurements, and Fractional Linear ($\langle L/I \rangle$) and Circular ($\langle |V|/I \rangle$) Polarization of Each 256 MHz Subband

Frequency (MHz)	τ_{sc} (ms)	S_ν (mJy)	$\langle L/I \rangle$	$\langle |V|/I \rangle$
3879	$\lesssim 3$	0.31 ± 0.03	0.73	0.19
3656	$\lesssim 3$	0.33 ± 0.01	0.94	0.18
3386	$\lesssim 3$	0.41 ± 0.01	0.86	0.18
3137	$\lesssim 1.9$	0.52 ± 0.01	0.88	0.20
2880	0.8 ± 0.5	0.62 ± 0.01	0.88	0.18
2612	1.2 ± 0.6	0.82 ± 0.01	0.92	0.16
2304	2.8 ± 0.5	1.11 ± 0.02	0.73	0.12
2106	3.5 ± 0.2	1.40 ± 0.01	0.92	0.11
1858	5.3 ± 0.2	1.79 ± 0.02	0.97	0.12
1598	8.8 ± 0.2	2.53 ± 0.01	0.93	0.11
1356	16.8 ± 0.2	3.72 ± 0.1	0.93	0.10
1070	38.6 ± 0.5	6.0 ± 0.1	0.83	0.16
809	186^{+7}_{-6}	11.8 ± 0.6	0.52	0.18

Note. The uncertainties denote the 68% confidence intervals. Only upper limits are set on the scattering timescale at frequencies above 2880 MHz and are with 68% confidence.

the point where we could only recover upper limits for scattering in subbands above 2106 MHz. As the profile width does not appear to undergo significant evolution with frequency, aside from scatter broadening, we refit the subbanded data assuming Gaussian priors of $\pi(\sigma_1) \sim \mathcal{N}(8\text{ ms}, 1\text{ ms})$ and $\pi(\sigma_2) \sim \mathcal{N}(7\text{ ms}, 1\text{ ms})$ for the widths of G_1 and G_2, respectively.

The resulting scattering timescale and period-averaged flux density—measured by averaging the best-fit template for each subband in pulse phase—are presented in Table 1. We measure a scattering timescale referenced to 1 GHz of $\tau_{sc,1\text{ GHz}} = 42^{+9}_{-3}$ ms, with a scattering index of $\alpha_{sc} = -3.4^{+0.3}_{-0.2}$. Similar but less well constrained values of $\alpha_{sc} = 3.6^{+0.8}_{-1.1}$ and $\tau_{sc,1\text{ GHz}} = 41^{+19}_{-18}$ ms were obtained when we used uniform priors on the widths of G_1 and G_2. In either case, the scattering timescale is consistent with the expected value of 62 ± 30 ms from the NE2001 galactic electron density model at 1 GHz (Cordes & Lazio 2002). While the scattering index is smaller than the expected value of $\alpha_{sc} = -4$ or $\alpha_{sc} = -4.4$ from Kolmogorov turbulence, they are consistent with the scattering indices of many other pulsars (see, e.g., Geyer et al. 2017). We also fit the period-averaged flux density spectrum using a simple power-law function, $S_\nu \propto \nu^\alpha$, obtaining a spectral index of $\alpha = -2.26^{+0.02}_{-0.03}$. The fits to the spectral index and scattering timescale are plotted in Figure 2. The reduced χ^2 for the scattering relation shown in Figure 2 is 13.8. We attribute the high value to overestimation of the scattering timescale in the RFI-affected 809 MHz band. Removing the 809 MHz data point confirms this suspicion, as refitting the scattering relation returns a consistent scattering index of $\alpha = -3.6^{+0.4}_{-0.3}$ and a reduced χ^2 of 0.6.

2.2. Polarimetry

Figure 1 clearly shows the linear polarization has undergone significant Faraday rotation, as evidenced by the large number of changes in sign for Stokes Q and U. Following the Bayesian methodology presented in Bannister et al. (2019), we measured

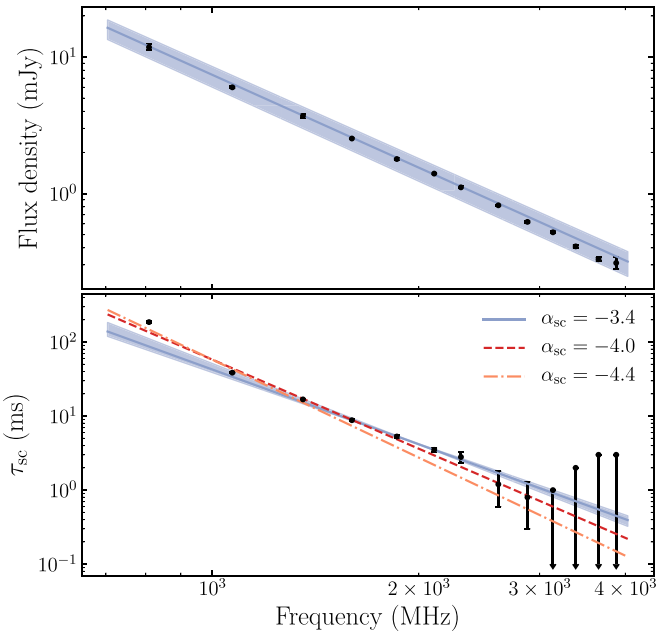

Figure 2. Period-averaged flux density (top) and scattering timescale (bottom) as functions of frequency. The blue solid lines indicate the median fit, while the shaded region is bounded by the 68% confidence intervals. Dashed red and dashed–dotted orange lines correspond to scattering indices of −4 and −4.4, respectively.

the phase-averaged rotation measure (RM) of the magnetar by directly fitting Stokes Q and U as a function of frequency, obtaining a value of $1442.0 \pm 0.2\text{ rad m}^{-2}$ (68% confidence interval). Note, this measurement does not include corrections for the ionosphere that can often exceed our measurement uncertainty. At Parkes, the ionospheric contribution is typically between -0.2 and -2.0 rad m^{-2} (Han et al. 2018).

To better visualize the polarization profiles, we plot the averaged polarization pulse profiles at 13 frequencies in Figure 3, along with the linear polarization position angle for each subband. The pulse profile is more than 90% linearly polarized across most of the UWL band, although a small amount of circular polarization is also present. Apparent depolarization due to scatter broadening (Li & Han 2003) is evident below 1356 MHz. Slight variations in the fractional linear and circular polarizations listed in Table 1 likely result from a combination of noise and polarization impurities in the receiver system. The apparent depolarization in the 2304 MHz band is an artifact of residual RFI from wireless communications contaminating the narrow strip of nonexcised channels between 2380 and 2400 MHz. Additionally, the lack of polarization in the "bump" visible in the off-pulse noise of the 3879 MHz subband suggests this feature is likely to be residual impulsive RFI, not an additional profile component. There is a slight upward slope in the linear polarization position angle (PA), with little frequency-dependent evolution except for scatter-induced smearing at lower frequencies.

2.3. Single Pulses

To analyze the single pulses from the magnetar, we created single-pulse archives from the original `psrfits` search-mode filterbank. We then performed a boxcar search for single pulses on copies of these archives where all frequency channels outside the 1300–2500 MHz band had been excised to minimize confusion with RFI. We limited this search to only

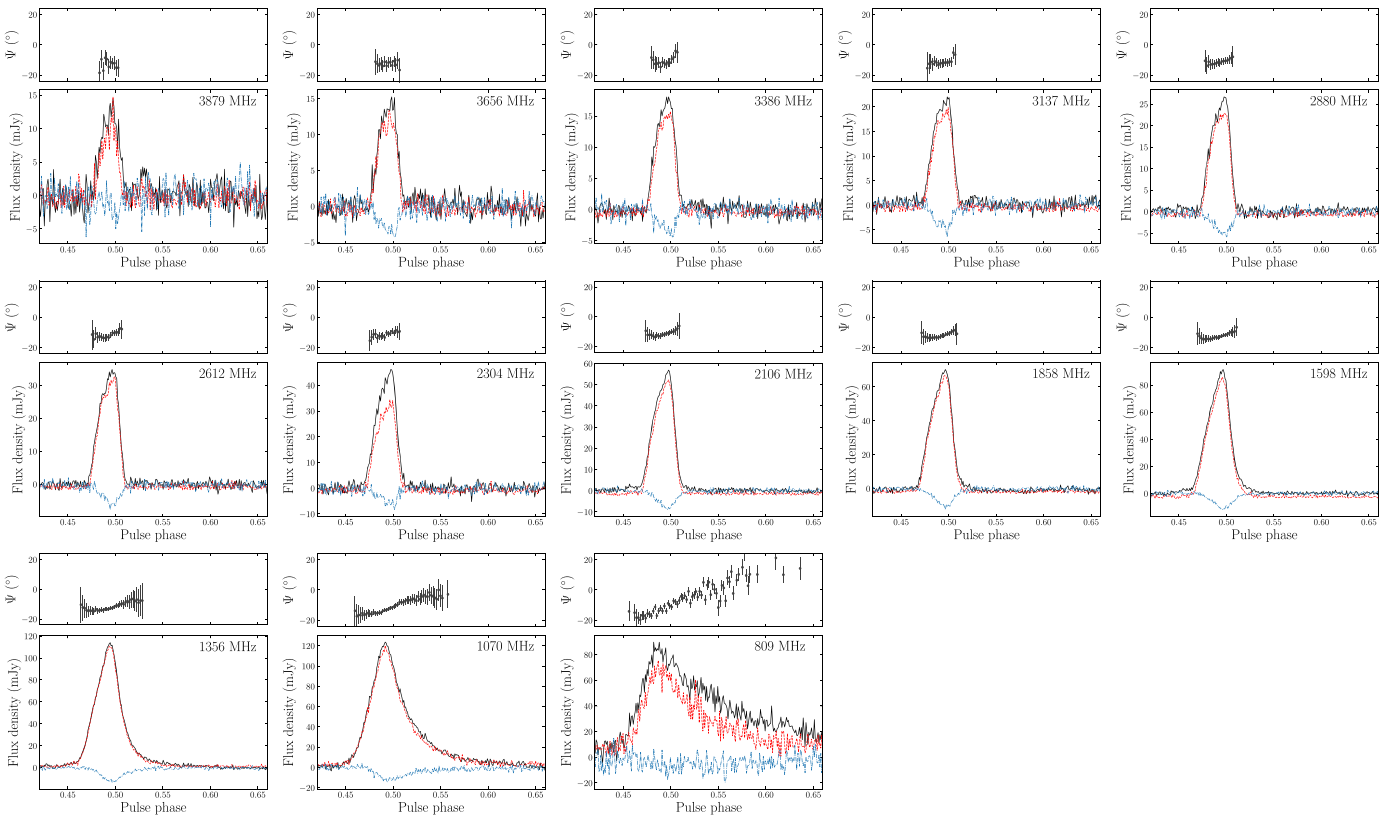

Figure 3. Polarization profiles of Swift J1818.0−1607 averaged over 13 subbands from 3656 MHz to 809 MHz, each dedispersed at a DM of 706 pc cm^{-3} and covering 256 MHz of bandwidth. Black represents total intensity, red is linear polarization, and blue is circular polarization. The linear polarization position angles (Ψ) are corrected for the RM = 1442.0 ± 0.2 rad m^{-2} at a reference frequency of 2368 MHz.

the on-pulse region of each archive. Applying a maximum boxcar width of 85 ms and threshold S/N of 7, we find 5052 of the 7008 single-pulse archives contained a single-pulse candidate that met our criterion with a median signal-to-noise ratio (S/N) of 13.8. Upon visual inspection, we found the single pulses typically consist of 1–3 "spiky" subpulses with similar phenomenology to single pulses seen from the four other radio-loud magnetars. We did not observe any single pulses emitted at rotational phases outside the "on-pulse" region represented by the integrated profiles in Figure 3, nor evidence of sporadic pulses from the additional profile component reported by Maan & van Leeuwen (2020). Occasional gaps or nulls in emission were seen throughout the observation. Similar behavior has been reported in observations of the galactic center magnetar SGR J1745 −2900 (Yan et al. 2018). However, it is not clear whether the gaps we observed represent true nulls, where the radio emission mechanism completely shuts off, or if the radio pulses during these rotations were simply below the detection threshold of the receiver.

We measured the flux density of the on- and off-pulse regions of each single-pulse archive using the `psrflux` tool from `PSRCHIVE` by cross-correlating the data with a scatter-broadened Gaussian template. Both the on- and off-pulse flux density measurements were then converted to units of matched-filter S/N by scaling each measurement by a factor of 1.4—the scale factor needed to scale the off-pulse distribution such that it has a mean of zero and variance of one. The resulting on- and off-pulse S/N distributions are shown in Figure 4. We note this definition of S/N is different to the one used in the earlier

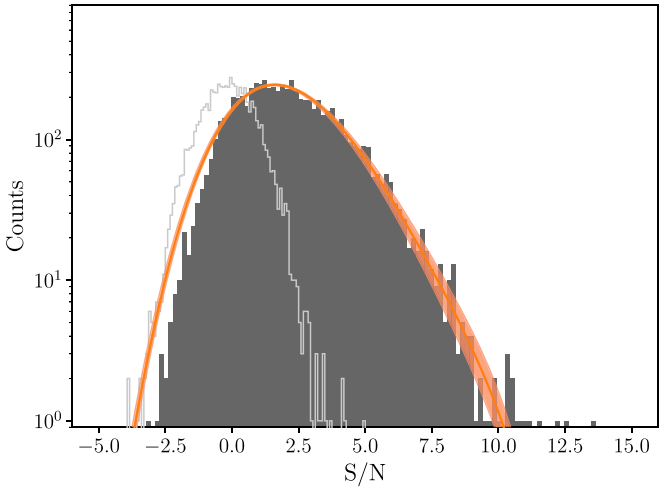

Figure 4. Matched-filter S/N distribution for the frequency-averaged single pulses (dark gray), scaled such that the off-pulse noise (light gray) has zero mean and unit variance. The orange line and shading are the median log-normal convolved with a Gaussian fit to the data and associated 68% confidence intervals.

single-pulse search, which was a top-hat S/N used to place quantitative constraints on the number of single pulses we detected. Negative S/N ratios can be attributed to the on-pulse flux being below zero due to fluctuations in the baseline. The on-pulse distribution is well described by a log-normal with a log-mean of 1.925 ± 0.003 and width of 0.25 ± 0.01 that has been convolved with a Gaussian distribution with zero mean and unit variance. This distribution width is typical of the

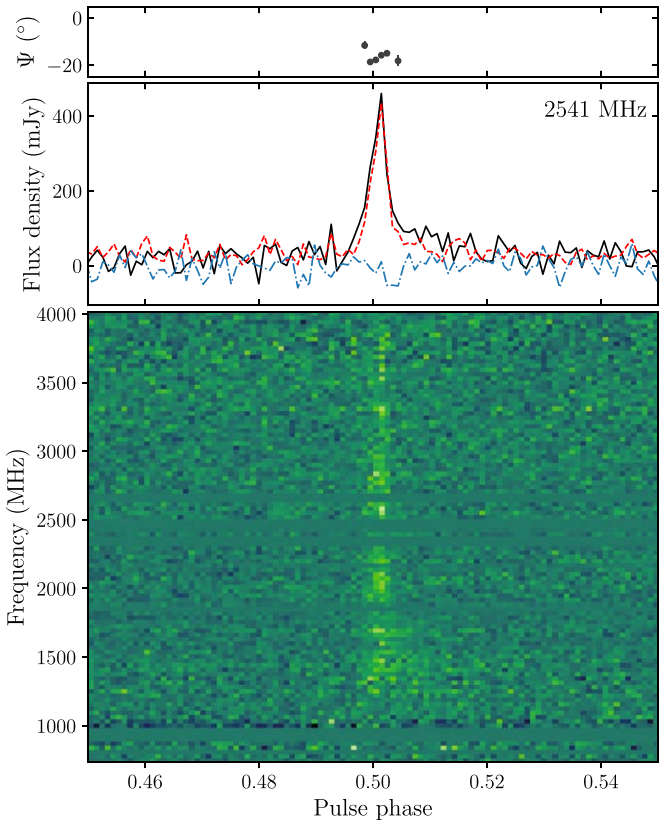

Figure 5. A single pulse from Swift J1818.0−1607. The top and middle panels show the position angle and integrated polarization profile. The bottom panel shows the waterfall diagram of the pulse dedispersed at a DM = 707.3 ± 0.2 pc cm^{-3} with 0.67 ms time resolution and 16 MHz spectral resolution.

rotation-powered pulsar population as a whole (Burke-Spolaor et al. 2012). While there are some outliers, the lack of a power-law tail in the distribution indicates no giant pulses were detected during our observation, contradictory to the claim by Esposito et al. (2020) that the single pulses are dominated by sporadic giant pulses. It is possible their giant pulse detections originated from the transient profile component seen in early observations by Maan & van Leeuwen (2020), which had disappeared sometime prior to our observation with Parkes.

The narrow widths of magnetar single pulses and subpulses enable high-accuracy DM measurements, particularly when observed across large bandwidths. For example, the bright single pulse shown in Figure 5 returned a structure-optimized DM of 707.3 ± 0.2 pc cm^{-3}. Repeating this for the brightest 215 single pulses in our sample, we find the distribution of structure-optimized DMs is well described by a Gaussian with a mean of 706.0 pc cm^{-3} and a standard deviation of 2.6 pc cm^{-3}. From this, we estimated the magnetar's DM to be 706.0 ± 0.2 pc cm^{-3} where the uncertainty is derived from the standard deviation of the DM distribution $\sigma_{\rm DM} = 2.6/(215-2)^{1/2}$ pc cm^{-3}. The variations in DM are more likely to have resulted from systematic errors in the structure-optimization algorithm combined with the variable number of subpulses in each pulse as opposed to short-timescale variations in the local environment of the magnetar. Long-term monitoring over year-long timescales will reveal if Swift J1818.0−1607 experiences DM variations similar to those seen in repeating FRBs (e.g., Hessels et al. 2019).

Using the NE2001 (Cordes & Lazio 2002) and YMW16 (Yao et al. 2017) galactic free electron density models, the distance to the magnetar is estimated to be either 8.1 ± 1.6 kpc (NE2001) or 4.8 kpc (YMW16), where the uncertainty is dominated by the model chosen.

From our measurements of both the RM and DM, we can estimate the average parallel magnetic field strength along the line of sight to the magnetar using the equation $B_{\parallel} = 1.2{\rm RM}/{\rm DM}$, where $B_{\parallel}$ is in units of μG, and the RM and DM are in their usual units (rad m^{-2} and pc cm^{-3}). Our measured value of 2.5 μG is fairly typical of line-of-sight $B_{\parallel}$ measurements from pulsars within the galactic plane (Han et al. 2018)

3. Discussion

In general, the pulsed radio emission from Swift J1818.0−1607 shares a lot of the same phenomenology seen in other radio-loud magnetars: a high degree of linear polarization, burst-like subpulses, and extremely variable pulse-to-pulse flux densities. However, the steep spectral index we measure is more consistent with the spectral indices of many rotation-powered pulsars when compared to the flat spectral indices of the four other radio magnetars that typically range between −0.5 and +0.3 (Lazaridis et al. 2008; Torne et al. 2015; Dai et al. 2019), making this new magnetar a significant outlier. Given the DM and location of the magnetar, the effects of diffractive interstellar scintillation are negligible at the UWL observing band. For instance, the NE2001 model predicts a scintillation bandwidth of only 3^{+3}_{-1} Hz at 1 GHz. Hence the steep spectrum is intrinsic to Swift J1818.0−1607. This indicates that it was premature to assume that all radio magnetars have flat spectra. At the large DMs typical of magnetars, those that have steep radio spectra might be so scatter broadened as to induce a significant selection effect toward those with flatter spectra. When compared to the 276 pulsars in Jankowski et al. (2018) that have spectra best fit by a simple power law, only ∼11% of pulsars have steeper spectra than Swift J1818.0−1607, while the four other radio magnetars all have spectral indices that are flatter than ∼94% of their sample. Hence, Swift J1818.0−1607 may be an example of the diversity that could exist in the wider, as-of-yet undetected radio magnetar population. The spectral properties could also be related to the magnetar possessing a less evolved magnetic field structure due to its youth.

Assuming Swift J1818.0−1607 was born rapidly rotating ($P \sim 10$ ms) and its spin-down is dominated by magnetic dipole radiation (braking index = 3), measurements of its spin and spin-down place its characteristic age between only 240 and 310 yr (Champion et al. 2020; Esposito et al. 2020; Hu et al. 2020), the second smallest of any pulsar after SGR J1806−20 (Mereghetti et al. 2005). However, given the large amount of uncertainty surrounding neutron star rotation periods at birth and the diversity in measured pulsar (and magnetar) braking indices, its true age is likely to be significantly different than the inferred spin-down age. Indeed the period derivatives of magnetars can change by large factors within just a few years (see, e.g., Scholz et al. 2017). A more accurate kinematic age could be inferred from associating the magnetar to a progenitor supernova remnant, combined with a proper-motion measurement from very long baseline interferometry. However, we find there are no cataloged supernova remnants or pulsar-wind nebula co-located with its position (Green 2019). The two

closest supernova remnants (G014.3+0.1 and G014.1−0.1) are approximately 19′ and 27′ away from the position of the magnetar on sky (Galactic coordinates: $l = 14.^{\circ}8$, $b = -0.^{\circ}14$), respectively, making an association highly unlikely. The lack of an associated supernova remnant is not too surprising, as only 8 of the 23 known magnetars have claimed associations. Additionally, the strong spin-down powered wind from newborn magnetars can accelerate the remnant expansion to the point that only anomalously diffuse shells, or no remnant at all, remains on century-long timescales (Duncan & Thompson 1992). If the progenitor supernova remnant has not been dissipated, then deep radio and X-ray imaging may be able to detect it.

Alternatively, we speculate the steep spectrum and its unusually faint X-ray luminosity of 7×10^{34} erg s^{-1} (Esposito et al. 2020)[5] may be evidence this new magnetar was initially born as a rotation-powered pulsar that obtained the rotational properties of a magnetar over time, similar to what is predicted for PSR J1734−3333 (Espinoza et al. 2011). Such evolution can occur if the magnetic and spin axes underwent rapid alignment over time (Johnston & Karastergiou 2017), or if the pulsar underwent an extended period of magnetic field growth after the surface magnetic field was initially buried due to fall-back accretion (e.g., Ho 2015).

If the properties of Swift J1818.0−1607 are the result of rapid magnetic and spin axes alignment, we would expect the PA to be consistent with that of an aligned rotator. There is some evidence magnetars tend toward aligned spin and magnetic axes. Both 1E 1547.0−5408 and PSR J1622−4950 have PA swings that are consistent with being aligned rotators (Camilo et al. 2008; Levin et al. 2012). This is further backed up by the wide radio profiles, and low pulsed X-ray fractions of these two magnetars (Halpern et al. 2008; Camilo et al. 2018). There is some ambiguity as to whether the spin and magnetic axes of XTE J1810−197 are aligned or orthogonal, as Camilo et al. (2007b) found both scenarios adequately describe the PA swing across its main pulse and inter-pulse. Conversely, Kramer et al. (2007) found that an offset dipole described by two separate rotating vector models (RVMs; Radhakrishnan & Cooke 1969) could also describe its PA behavior, and speculated it may be evidence for XTE J1810−197 having a multipole magnetic field. Additionally, Dai et al. (2019) observed distinctly non-RVM PA variations following its 2018 outburst. For Swift J1818.0−1607, the flat PA in the higher-frequency panels of Figure 3 is broadly consistent with the RVM for a dipole magnetic field. However, the narrow pulse duty cycle makes it difficult to constrain the star's magnetic geometry, as the relatively flat PA could be consistent with either nearly aligned magnetic and spin axes, or a large offset between the magnetic axis and our line of sight. Given the radio profiles of magnetars evolve over the weeks to months following an outburst (Kramer et al. 2007; Dai et al. 2019), it may be possible to measure the magnetic geometry of Swift J1818.0−1607 in the future.

Pulsars that experienced fall-back accretion soon after their birth can undergo apparent magnetic field growth as their magnetic fields diffuse to the surface over time (see, e.g., Muslimov & Page 1995). This can result in a seemingly "normal" rotation-powered, young pulsar obtaining magnetar-like rotational properties within ∼1–10 kyr (Ho 2015). If Swift J1818.0−1607 is a result of this evolutionary path, then we may expect it to show similar radio properties to the high B-field PSRs J1119−6127, J1208−6238, and J1846−0258. While PSRs J1846−0258 (Gavriil et al. 2008) and J1119−6127 (Archibald et al. 2016) have been observed to undergo magnetar-like outbursts in the past, only PSR J1119−6127 has been observed to emit radio pulses. Observationally, we can draw parallels between the radio properties of Swift J1818.0−1607 and those of PSR J1119−6127 during its 2016 outburst. Following the initial suppression and reemergence of radio pulses from PSR J1119−6127, multiband flux measurements found the pulsar possessed a steeper radio spectrum than its nominal $\alpha = -1.4 \pm 0.2$, with values of α ranging between -2.2 ± 0.2 and -1.9 ± 0.2 (Majid et al. 2017). Later observations found its radio spectrum had undergone spectral flattening to a more magnetar-like spectral index of -0.52 ± 0.06 over the months following the outburst (Pearlman et al. 2016). The flux density of PSR J1119−6127 also underwent a factor of 5 increase in two weeks after the outburst before recovering back to its normal levels (Dai et al. 2018). In addition to having a comparably steep post-outburst spectral index, Swift J1818.0−1607 appears to have also undergone a similar radio brightening, as the flux densities at 1356 and 1598 MHz in Table 1 are a factor of 5–12 times higher than measurements at similar observing frequencies two weeks prior to our Parkes UWL observation (Esposito et al. 2020; Karuppusamy et al. 2020; Lower & Shannon 2020). The refractive modulation timescale is expected to be very long (years) and the modulation index to be low (Cordes & Lazio 2002). Thus the increase in flux density cannot be ascribed to refractive effects. If the current outburst of Swift J1818.0−1607 continues to proceed in a similar manner to the 2016 outburst of PSR J1119−6127, then we may expect the steep spectral index to undergo a similar flattening and for the flux density to decay to a more steady state over the coming months. A more recent spectral index measurement of $\alpha = -1.9 \pm 0.2$ from multiband observations (Majid et al. 2020) suggests some amount of spectral flattening may have already occurred. Continued monitoring with multiband and wide-bandwidth receiver systems will either confirm the spectral index is flattening toward a more magnetar-like value, or is simply fluctuating about some mean value. Additionally, a measurement of the braking index would allow us to understand the future spin and magnetic field evolution of the magnetar and potentially confirm or rule out a rotation-powered pulsar origin.

The Parkes radio telescope is part of the Australia Telescope National Facility, which is funded by the Australian Government for operation as a National Facility managed by CSIRO. We acknowledge the Wiradjuri people as the traditional owners of the Observatory site. This work made use of the OzSTAR national HPC facility, which is funded by Swinburne University of Technology and the National Collaborative Research Infrastructure Strategy (NCRIS). This work was supported by the Australian Research Council (ARC) Laureate Fellowship FL150100148 and the ARC Centre of Excellence CE170100004 (OzGrav). M.E.L. receives support from the Australian Government Research Training Program and CSIRO Astronomy and Space Science. R.M.S. is supported

[5] As noted in Esposito et al. (2020), the quoted X-ray luminosity assumes the smaller, YMW16 DM distance to the magnetar, and that a larger source distance (as implied by the NE2001 model) may yield a more normal luminosity.

through ARC Future Fellowship FT190100155. We thank Shi Dai for useful discussions and suggestions on calibrating the UWL data. We are grateful to the ATNF staff, in particular James Green, for allocating us time to perform this observation. We also thank the anonymous referee for helpful comments and suggestions. This work made use of the Astronomer's Telegram and NASA's Astrophysics Data Service.

Software: `bilby` (Ashton et al. 2019), `clfd` (Morello et al. 2019), `cmasher` (van der Velden 2020), `DM_phase` (Seymour et al. 2020), `dspsr` (van Straten & Bailes 2011), `matplotlib` (Hunter 2007), `numpy` (Oliphant 2006), `PSRCHIVE` (Hotan et al. 2004; van Straten et al. 2012).

ORCID iDs

Marcus E. Lower https://orcid.org/0000-0001-9208-0009
Ryan M. Shannon https://orcid.org/0000-0002-7285-6348
Simon Johnston https://orcid.org/0000-0002-7122-4963
Matthew Bailes https://orcid.org/0000-0003-3294-3081

References

Archibald, R. F., Kaspi, V. M., Tendulkar, S. P., & Scholz, P. 2016, ApJL, 829, L21
Ashton, G., Hübner, M., Lasky, P. D., et al. 2019, ApJS, 241, 27
Bannister, K. W., Deller, A. T., Phillips, C., et al. 2019, Sci, 365, 565
Burke-Spolaor, S., Johnston, S., Bailes, M., et al. 2012, MNRAS, 423, 1351
Camilo, F., Ransom, S. M., Halpern, J. P., et al. 2006, Natur, 442, 892
Camilo, F., Ransom, S. M., Halpern, J. P., & Reynolds, J. 2007a, ApJL, 666, L93
Camilo, F., Reynolds, J., Johnston, S., et al. 2007b, ApJL, 659, L37
Camilo, F., Reynolds, J., Johnston, S., Halpern, J. P., & Ransom, S. M. 2008, ApJ, 679, 681
Camilo, F., Scholz, P., Serylak, M., et al. 2018, ApJ, 856, 180
Champion, D., Desvignes, G., Jankowski, F., et al. 2020, ATel, 13559, 1
Cordes, J. M., & Lazio, T. J. W. 2002, arXiv:astro-ph/0207156
Dai, S., Johnston, S., Weltevrede, P., et al. 2018, MNRAS, 480, 3584
Dai, S., Lower, M. E., Bailes, M., et al. 2019, ApJL, 874, L14
Duncan, R. C., & Thompson, C. 1992, ApJL, 392, L9
Eatough, R. P., Falcke, H., Karuppusamy, R., et al. 2013, Natur, 501, 391
Enoto, T., Sakamoto, T., Younes, G., et al. 2020, ATel, 13551, 1
Espinoza, C. M., Lyne, A. G., Kramer, M., Manchester, R. N., & Kaspi, V. M. 2011, ApJL, 741, L13
Esposito, P., Rea, N., Borghese, A., et al. 2020, ApJL, 896, L30
Evans, P. A., Gropp, J. D., Kennea, J. A., et al. 2020, GCN, 27373, 1
Gajjar, V., Perez, K., Siemion, A., et al. 2020, ATel, 13575, 1
Gavriil, F. P., Gonzalez, M. E., Gotthelf, E. V., et al. 2008, Sci, 319, 1802
Geyer, M., Karastergiou, A., Kondratiev, V. I., et al. 2017, MNRAS, 470, 2659
Green, D. A. 2019, JApA, 40, 36
Halpern, J. P., Gotthelf, E. V., Reynolds, J., Ransom, S. M., & Camilo, F. 2008, ApJ, 676, 1178
Han, J. L., Manchester, R. N., van Straten, W., & Demorest, P. 2018, ApJS, 234, 11
Hessels, J. W. T., Spitler, L. G., Seymour, A. D., et al. 2019, ApJL, 876, L23
Ho, W. C. G. 2015, MNRAS, 452, 845
Hobbs, G., Manchester, R. N., Dunning, A., et al. 2020, PASA, 37, e012
Hotan, A. W., van Straten, W., & Manchester, R. N. 2004, PASA, 21, 302
Hu, C.-P., Strohmayer, T. E., Ray, P. S., et al. 2020, ATel, 13588, 1
Hunter, J. D. 2007, CSE, 9, 90
Jankowski, F., van Straten, W., Keane, E. F., et al. 2018, MNRAS, 473, 4436
Johnston, S., & Karastergiou, A. 2017, MNRAS, 467, 3493
Karuppusamy, R., Desvignes, G., Kramer, M., et al. 2020, ATel, 13553, 1
Kramer, M., Stappers, B. W., Jessner, A., Lyne, A. G., & Jordan, C. A. 2007, MNRAS, 377, 107
Lazaridis, K., Jessner, A., Kramer, M., et al. 2008, MNRAS, 390, 839
Levin, L., Bailes, M., Bates, S., et al. 2010, ApJL, 721, L33
Levin, L., Bailes, M., Bates, S. D., et al. 2012, MNRAS, 422, 2489
Li, X. H., & Han, J. L. 2003, A&A, 410, 253
Lower, M. E., & Shannon, R. M. 2020, ATel, 13587, 1
Maan, Y., & van Leeuwen, J. 2020, ATel, 13560, 1
Majid, W. A., Pearlman, A. B., Dobreva, T., et al. 2017, ApJL, 834, L2
Majid, W. A., Pearlman, A. B., Prince, T. A., et al. 2020, ATel, 13649, 1
McLaughlin, M. A., Lyne, A. G., Lorimer, D. R., et al. 2006, Natur, 439, 817
Mereghetti, S., Tiengo, A., Esposito, P., et al. 2005, ApJ, 628, 938
Morello, V., Barr, E. D., Cooper, S., et al. 2019, MNRAS, 483, 3673
Muslimov, A., & Page, D. 1995, ApJL, 440, L77
Olausen, S. A., & Kaspi, V. M. 2014, ApJS, 212, 6
Oliphant, T. 2006, NumPy: A Guide to NumPy (Spanish Fork, UT: Trelgol Publishing) http://www.numpy.org/
Pearlman, A. B., Majid, W. A., Horiuchi, S., et al. 2016, ATel, 9870, 1
Pearlman, A. B., Majid, W. A., Prince, T. A., Kocz, J., & Horiuchi, S. 2018, ApJ, 866, 160
Radhakrishnan, V., & Cooke, D. J. 1969, ApL, 3, 225
Scholz, P., Camilo, F., Sarkissian, J., et al. 2017, ApJ, 841, 126
Seymour, A., Michilli, D., & Pleunis, Z. 2020, DM_phase, GitHub, https://github.com/danielemichilli/DM_phase
Shannon, R. M., & Johnston, S. 2013, MNRAS, 435, L29
Speagle, J. S. 2020, MNRAS, 493, 3132
Torne, P., Eatough, R. P., Karuppusamy, R., et al. 2015, MNRAS, 451, L50
van der Velden, E. 2020, JOSS, 5, 2004
van Straten, W., & Bailes, M. 2011, PASA, 28, 1
van Straten, W., Demorest, P., & Oslowski, S. 2012, AR&T, 9, 237
Weltevrede, P., Johnston, S., & Espinoza, C. M. 2011, MNRAS, 411, 1917
Yan, W. M., Wang, N., Manchester, R. N., Wen, Z. G., & Yuan, J. P. 2018, MNRAS, 476, 3677
Yao, J. M., Manchester, R. N., & Wang, N. 2017, ApJ, 835, 29